FINIS: A COMPACT IMAGING SPECTROMETER FOR METHANE PLUME DETECTION

Bruno Mattos[1], **Michael Kirk**[1], **Alan Marchant**[1], **Charles Swenson**[1], **Mark Schoeberl**[2], ***Lucas Anderson***[3]

[1]*Utah State University, Center for Space Engineering, 4130 Old Main Hill, Logan, Utah 84321*

[2]*Science and Technology Corporation, 10015 Old Columbia Road, E-250, Columbia, MD 21046*

[3]*Orion Space Solutions, 282 Century Place, 1000, Louisville, CO 80027*

ABSTRACT

Space-based imaging spectrometers play a critical role in monitoring greenhouse gas emissions, particularly methane. This paper provides updates on the development of the Filter Incidence Narrow-band Infrared Spectrometer (FINIS), a compact imaging spectrometer designed for methane plume detection. Through an innovative design that uses tilted interference filters in a binocular configuration, FINIS offers competitive methane measurement capabilities in terms of precision and spatial resolution while maintaining a compact form factor and low power requirements. This work covers the instrument parameters and its operation concept. A retrieval simulation using synthesized images in a scenario with the presence of varying sizes of plumes shows that FINIS can potentially detect point sources with leak rates exceeding 500 kg/h under specified conditions. Additionally, the results of a calibration test using a methane cell are presented, validating the instrument's modeled spectral response and central wavelength mapping. FINIS is slated for space testing as one of the student payloads aboard the upcoming ACMES mission, a 16U CubeSat selected under NASA's In-space Validation of Earth Science Technologies (InVEST) program, expected to launch in 2025.

1 INTRODUCTION

Monitoring methane emissions from space has assumed paramount importance in mitigating the acceleration of global warming. Since 1750, the average surface concentration of CH_4 has surged by over 150%, peaking at 1934 parts per billion (ppb) by November of 2023 [1], primarily propelled by anthropogenic activities. The impact of methane emissions on global warming surpasses that of carbon dioxide, with a Global Temperature change Potential (GTP) 70 times greater in the short term (20 years) and 11 times greater in the long term (100 years), factoring in climate-carbon feedbacks [2]. Anthropogenic methane emissions are predominantly attributed to the Energy, Livestock, and Waste Management sectors. The detection and measurement of methane emissions from sources such as landfills, coal mines, and oil and natural gas facilities is achievable through airborne or space-based imaging spectrometers. These instruments enable the detection of plumes, which are delineated as regions exhibiting a notably higher estimated vertical column concentration of methane compared to the surrounding background.

Students of the Utah State University (USU) are leading the development of a new infrared imaging spectrometer designed to capture the enhancement of methane concentrations in plumes relative to the background. The device is compact and low-power, and it is primarily made up of commercial-of-the-shelf (COTS) components, which makes it a promising feasible option for a large-scale application in nanosatellite constellations. This instrument is called Filter Incidence Narrow-band Infrared Spectrometer (FINIS), and it is scheduled to be tested in space onboard the Active Cooling for Multispectral Earth Sensors (ACMES) satellite, expected to be launched in 2025 [3]. ACMES is an

advanced 16U CubeSat mission selected under the In-space Validation of Earth Science Technologies (InVEST) Program in support of the NASA Science Mission Directorate.

This paper presents updates on the FINIS development, including an overview of the instrument's current design, onboard calibration unit, spectrum response, and operation concept. Additionally, it explains the proposed fast retrieval method for assessing the possible presence of plumes with less measurement accuracy, but with lower computational demand compared to optimal methods. This retrieval uses the log difference of the pair of frames acquired by FINIS to form the ground sample measurement vector, from which the relative methane concentration is retrieved by least square fitting. Furthermore, a plume detection simulation is conducted utilizing synthesized images based on Landsat-9 surface reflectance data and on the radiance computed considering a methane concentration mask containing Gaussian plumes of different leak rate sizes in the scene. Moreover, results from a methane cell calibration are presented to verify the center wavelength (CWL) distribution across the focal plane array (FPA). Lastly, more details are provided about the upcoming ACMES mission, which will host FINIS alongside three other crucial technologies for validation in space.

2 THE INSTRUMENT

To capture the spatial and spectral information of the scene, FINIS innovates by employing a tilted narrow-band interference filter (IF) at the entrance of its two imagers, as shown in Fig. 1. Since the filter bandpass CWL shifts as a function of the angle of incidence (AOI) of the incoming light, the spectral information can be acquired by taking a sequence of frames as the satellite passes over the target. With this approach, each frame captures the target at a different wavelength as its position translates across the field of view (FOV), changing the AOI [4]. The full spectrum of the target can be assembled by registering the stack of frames after image corrections are applied.

FINIS' scanning method is called windowing [5], and it is the same employed by the GHGSat satellites. However, unlike FINIS, the GHGSat spectrometer integrates a wide-angle Fabry-Pérot placed in the Fourier plane of the optical system [6], rather than employing an IF at the entrance. Both approaches offer significantly higher optical transmittance for instruments when compared to the more common dispersive push-broom spectrometers that use a diffraction grating, such as the TROPOMI[7], MethaneSAT[8], and CarbonMapper[9], or a prism as in the case of PRISMA[10]. While the optical transmittance of a typical diffraction grating-based spectrometer is typically less than 40% ([8],[9]), FINIS can achieve over 85% of optical transmittance in each imager due to its simple optical design that only uses one high transmission narrowband IF at the entrance, three AR coated lenses and one blocking filter in each telescope. This gives FINIS a significant light throughput advantage and allows it to deliver comparable signal-to-noise ratio (SNR) performance while maintaining a compact footprint, as shown in Table 1.

Table 1: FINIS - Size, Mass and Power

Parameter	Value	Unit
Instrument dimensions (H×W×L)	7.3×9.7×12.7	cm
Total mass	0.9	kg
Peak Power	11	W

Another innovation brought by FINIS is the use of a binocular system as depicted in Fig. 1. The two imagers have identical cameras and optical components, and share the same FOV. The sensor parameters are as listed in Table 2. The only difference between them is the tilt angle γ defined as the rotation around the y-axis. In the current design, the tilt angle of both filters has the same magnitude, 10°, but they are tilted in opposite directions, making the spectrum collected by CAM1 to be mirrored in CAM2, as shown by Fig. 2. No parallax is expected since the separation between the two imagers is negligible compared to the orbital altitude.

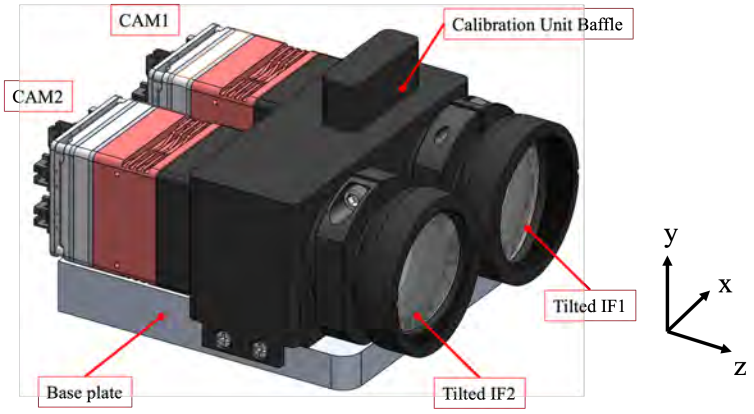

Figure 1: FINIS - CAD model in isometric view. The x,y, and z axes indicate the along-track, cross-track, and nadir directions, respectively.

Table 2: Parameters of a single imager

Parameter	Value	Unit
Spectral range	1659-1668	nm
Spectral resolution (FWHM)	1.5	nm
Pixel Size[a]	150×205	m
Swath[a]	96	km
Focal Plane Array	512×640	-
Detector size	15	μm
Clear aperture diameter	27	mm
F-number	2.04	-
Optical transmittance	>85%	-
Field of view cross-track	9.97	deg
Field of view in-track	7.98	deg
Instantaneous field of view	27.2	mrad
IF CWL at Normal Incidence	1672	nm
IF tilt angle (γ)	10	deg

a. Considering 550km orbital altitude.

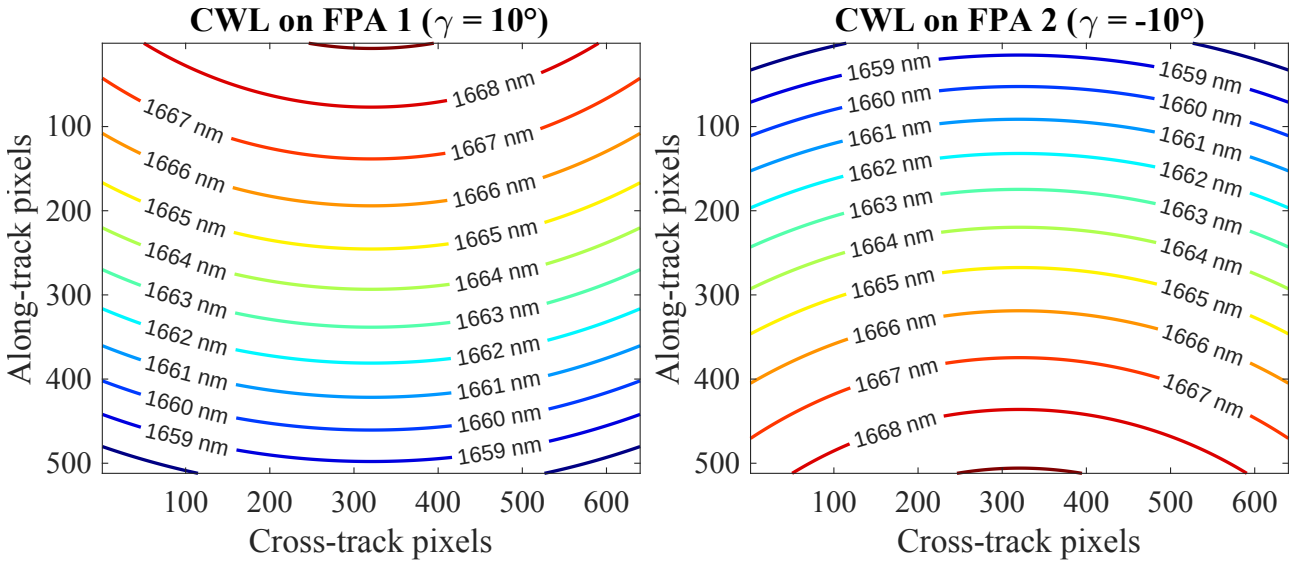

Figure 2: Center wavelength (CWL) across the FPA1 and FPA2 as the consequence of the tilted interference filter placed at the entrance of each aperture. γ is the tilt angle.

2.1 Onboard Calibration Unit

As illustrated in Fig. 3, FINIS is outfitted with a calibration unit designed for onboard dark frame and flat fielding calibration. This unit comprises a shutter with a double paddle, that blocks the light from reaching both detectors simultaneously when the self-restoring solenoid is energized. Once the shutter is closed, a sequence of dark frames and flat frames can be captured, employing the same exposure time and camera settings utilized during target frame acquisition. The resultant mean dark frame and flat frame are subsequently employed to rectify target frames in terms of dark counts and pixel gain (flat fielding), respectively.

For flat frame acquisition, each lens tube is equipped with an integrated LED ring composed of eight infrared LEDs. The brightness of these LEDs is regulated by a Pulse Width Modulation (PWM) signal. The emitted light is partially scattered within the tube and reflected by the shutter surface, which is coated with a Lambertian diffuser film.

The calibration unit is presently undergoing testing and characterization. The illumination pattern of the LED ring is being calibrated to determine the corrections required to compensate for any nonuniformities across the field. During flight operations, vicarious calibration targets will be used to monitor the flat fielding corrections, allowing adjustments for any changes in LED intensity induced by temperature fluctuations or radiation degradation.

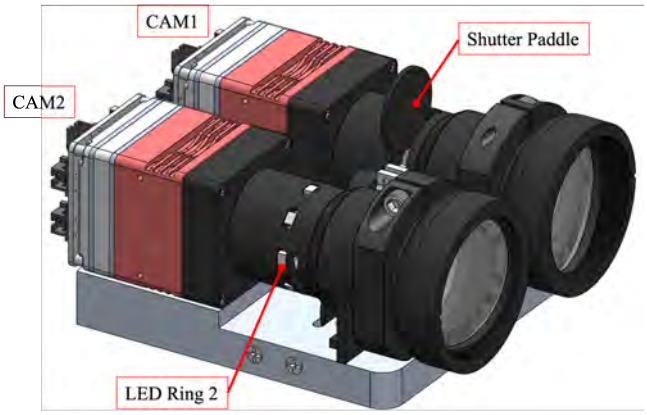

Figure 3: FINIS - onboard calibration uncovered by the baffle

3 RETRIEVAL METHOD FOR PLUME DETECTION

With the binocular setup, the measurement vector y can be defined as the natural log difference of the radiance measured by CAM1, L_1, and by CAM2, L_2, with the addition of the measurement noise, ϵ, as shown in Eq. (1), where the subscripts j and i denote the wavelengths measured by CAM2 and CAM1, respectively. Since CAM1 and CAM2 acquire measurements synchronously, the viewing geometry is the same for each pair of L_1 and L_2 measurements. This means that the measurement vector is independent of the surface reflectance function, which would otherwise need to be fitted using a low-order polynomial. Additionally, using the ratio of radiance measurements eliminates the need for absolute radiometric calibration since the radiometric conversion factor is also factored out.

$$y_{ij} = \ln \frac{L_1(\lambda_i)}{L_2(\lambda_j)} + \epsilon \tag{1}$$

While optimal estimation is essential for precisely retrieving the full-state vector, which includes methane and water vapor concentration, while considering factors like measurement noise and prior information [11], a fast retrieval approach is proposed for plume detection. This initial estimation

involves assuming methane concentration as the primary variable across the scene, while water vapor concentration remains either uniform or changes gradually. Under these conditions, the relative methane concentration can be calculated by assuming a linear relationship between the measurement vector y and the slant optical depth difference, $X_{ji} = \tau_j - \tau_i$, as expressed in Equation 2. This approximation also disregards the natural log difference of the solar spectrum irradiance for the pair of wavelengths, since the wavelength range covered by the sensor is less than 10 nm wide, and the solar spectrum (before passing through the atmosphere) is assumed to be approximately flat within that range.

$$y_{ij} = \alpha_{CH_4} X_{ji} + \epsilon \tag{2}$$

Considering the specific location and elevation of the target, along with the Solar Zenith Angle (SZA) during acquisition, the optical depth difference X_{ji} can be computed for a reference atmosphere and adjusted for the slant path. This computation can be executed using a Radiative Transfer Model (RTM), such as SCIATRAN [12]. Subsequently, the relative methane concentration α_{CH_4} can be estimated utilizing linear least square fitting, as outlined in Equation 3. Here, Y denotes the column vector of measurements y_{ij}, and X represents the predictor variable formed by the corresponding column vector of X_{ji}. In this case, the estimated methane concentration $\hat{\alpha}_{CH_4}$ is relative to the reference methane concentration used to compute X_{ji}.

$$\hat{\alpha}_{CH_4} = (X^T X)^{-1} X^T Y \tag{3}$$

The retrieval using this simplified method may introduce a bias originating from the disparity between the actual atmospheric state and the reference atmosphere and also from the albedo estimation error of the ground samples. However, by assuming a uniform distribution of water vapor, this bias tends to be uniformly spread across the scene, still enabling the detection of plumes by the regions of enhanced estimated concentration relative to their surroundings. Once a plume is detected within the scene, an optimal retrieval can be performed to accurately estimate the full-state vector. This second retrieval not only ensures a more precise estimation of the methane concentration but also verifies that the detected plume is indeed methane and not solely water vapor.

3.1 Methane Plume Detection Simulation with Synthesized Imagery

A simulation employing synthesized images was conducted to evaluate the instrument's capability in pinpointing plumes of varying sizes using the retrieval method discussed earlier. The baseline scenario image was constructed by combining two Landsat-9 Collection 2 Level 2 images, which encode surface reflectance (albedo) for each spectral band. Fig. 4-a depicts an RGB composite of the baseline image utilizing Bands 2, 3, and 4. Surface reflectance data utilized in the simulation was extracted from Band 6 (SWIR 1: 1.57-1.65μm).

A methane concentration mask was superimposed onto the entire scene, assuming a uniform background concentration of methane and water vapor. Within the scene's central region, a grid comprising 25 Gaussian-modeled plumes was introduced, as illustrated in Fig. 4-b. The plumes were arranged such that leak rates varied by row, with the top row exhibiting the highest leak rate of 5 metric tons per hour, followed by 3, 2, 1, and 0.5 t/h for the subsequent rows. In the Gaussian plume model, the atmosphere was deemed moderately unstable (stability class B, [13]), with surface reflection and near-surface wind speed set at 5 km/h from the northeast direction.

The ground scanning pattern depicted over the baseline image in Fig. 4-a was simulated based on a total acquisition time of 30 seconds, with each camera operating at 5 frames per second (fps), resulting in a total of 300 images from both imagers. The sensor was positioned in a 550km circular orbit with an inclination of 98 degrees, with the overpass occurring during the descending phase of the orbit (north to south). An exposure time of 8ms was utilized, resulting in a pixel size of 150m$\times$205m.

The scanning simulation also factored in the Earth's rotation computed for the target latitude, leading to the noticeable lateral motion towards the west of the footprints.

The image signals were initially generated utilizing the albedo information from the baseline scene, which was confined by the frame footprint. Subsequently, the cropped frames underwent downsampling to the instrument's spatial resolution, transitioning from the original square pixel of 30m to match the instrument's pixel size of 150m×205m.

The spectral radiance was simulated using SCIATRAN, assuming a Solar Zenith Angle (SZA) of 60 degrees and clear sky conditions. The computed radiance for each ground sample was then adjusted based on the deviation of methane concentration from the reference atmosphere, utilizing the methane weighting function also provided by the RTM. Following this, the output spectrum underwent convolution with the instrument function modeled as a Gaussian 1.5nm FWHM. It is anticipated that the instrument bandwidth remains invariant across the FPA since the incoming light can be regarded as collimated.

Once the spectral radiance was determined, the radiant flux on each detector was computed, taking into account the CWL distribution of each camera as presented in Fig. 2. Image noise was added assuming a Gaussian distribution, with the standard deviation calculated considering the camera noise parameters provided by the manufacturer (dark current and readout noise) combined with shot noise (square root of the signal). Finally, the images were blurred by the exposure motion and convolved with the instrument's modeled point spread function (PSF). Fig. 4-c displays the simulated image from CAM1 at the central frame of the stack, where the plumes were inserted.

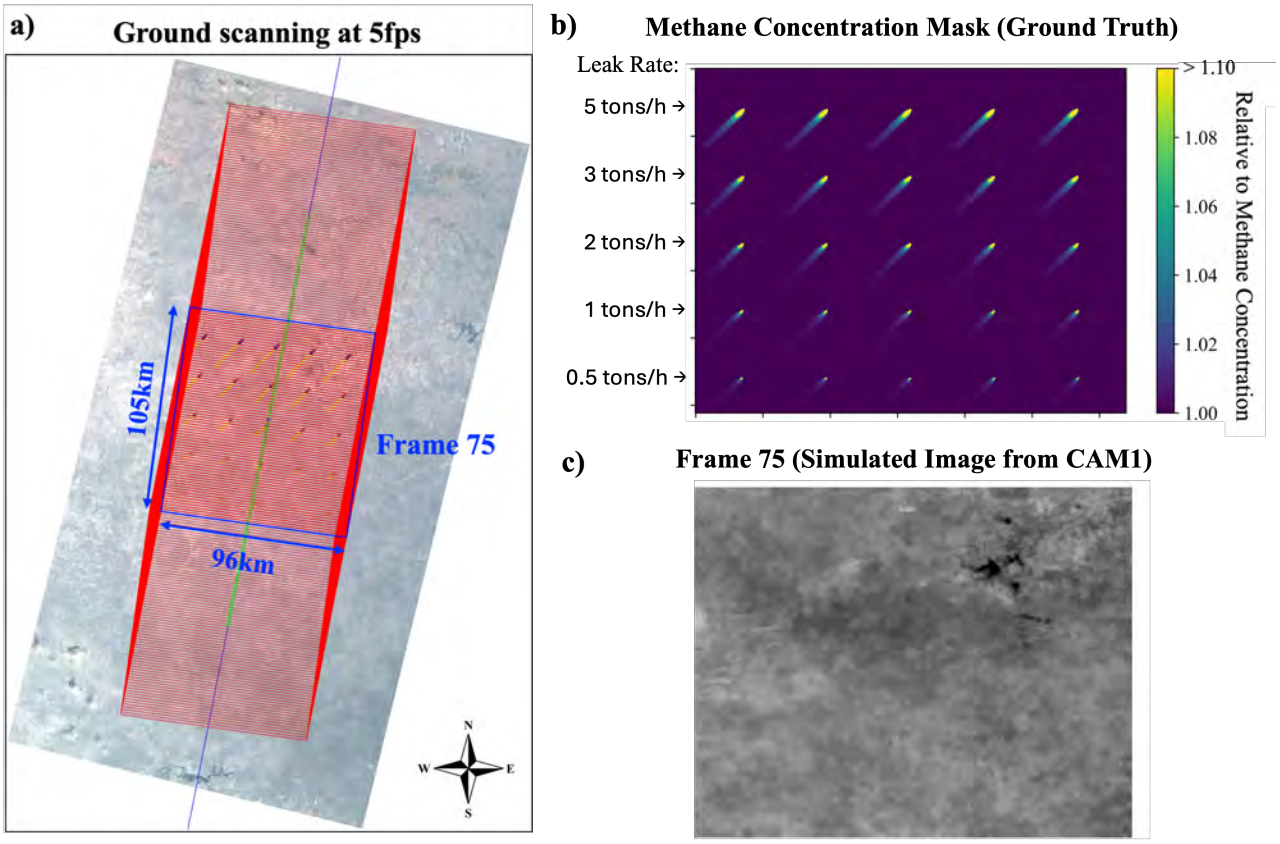

Figure 4: a) Baseline image of scenario showing CAM1 and CAM2 frames' footprint for 30s of acquisition time at 5fps. b) Methane concentration mask showing the Gaussian plumes arranged in a grid with leak rates across the rows ranging from 5 t/h in the first row to 0.5 t/h in the bottom row. c) Simulated frame 75 taken by CAM1 showing the location over which the plumes were inserted.

In the processing phase, the first step involved correcting the two stacks of 150 images from CAM1 and CAM2 by removing the estimated dark counts. Following this correction, the corrected stack of

frames, along with their corresponding CWL maps, underwent registration relative to the central frame. The registration was executed using a phase correlation-based method, which considered only translation and rotation between consecutive frames.

Once the registration process was completed, each ground sample's measurement vector y could be computed by calculating the natural log difference of the pair of frames from CAM1 and CAM2 and stacking them with the appropriate registration transformation. Subsequently, the first estimate of the relative methane concentration was derived through the application of linear least square-fitting, as defined in Eq. (3). The retrieval result is presented in Fig. 5 considering the nominal SNR (left) and for a scenario where the SNR ratio performance is a third of the expected from the nominal noise floor (right).

As observable in Fig. 5, in addition to highlighting the plumes, the retrieval erroneously indicates a high methane concentration over the lakes located in the upper right quarter of the scene. This issue arises from the water's low spectral albedo, but it can be easily addressed by masking out the ground samples that had low signal measurements from both CAM1 and CAM2 images.

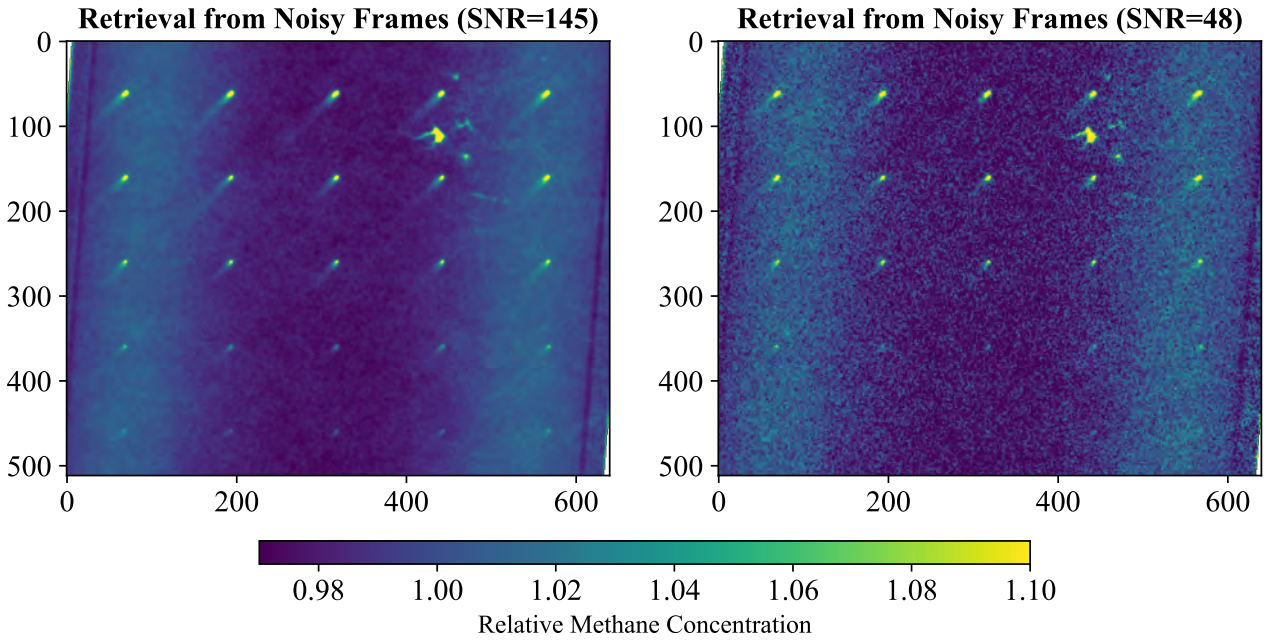

Figure 5: (left) Relative methane concentration map retrieval from frames with nominal noise performance. (right) Retrieval from frames with three times the noise expected from the sensor model.

The simulated retrieval shows promising results, considering that the scene's radiance level was computed for a solar zenith angle (SZA) of 60 degrees, which is considered the maximum SZA for FINIS operation. By examining Fig. 6, which presents a closer look at the retrieval along the middle column of plumes, we can compare the peak plume signals relative to the local background level. In the nominal retrieval, where the scene average SNR was computed to be 145, the plume signals from all tested leak rates showed peak levels higher than 3σ of the background average level. On the other hand, with the retrieval from the noisier frames (worst case), only the plumes with leak rates higher than 2 t/h can be unambiguously detected by the 3σ criteria. Moreover, although the retrieval presented a measurement bias that varies along the cross-track direction, visible by the two vertical wide stripes in the methane concentration map, all plumes across the same rows exhibited similar signals relative to the local background.

For the sake of comparison, Table 3 presents the point source detection thresholds of other space-based infrared spectrometers capable of measuring methane. It is evident that FINIS offers a detection performance on par with PRISMA and the recently deployed MethaneSAT. Despite its slightly coarser spatial resolution, FINIS boasts a swath eight times broader than GHGSat and three times wider than

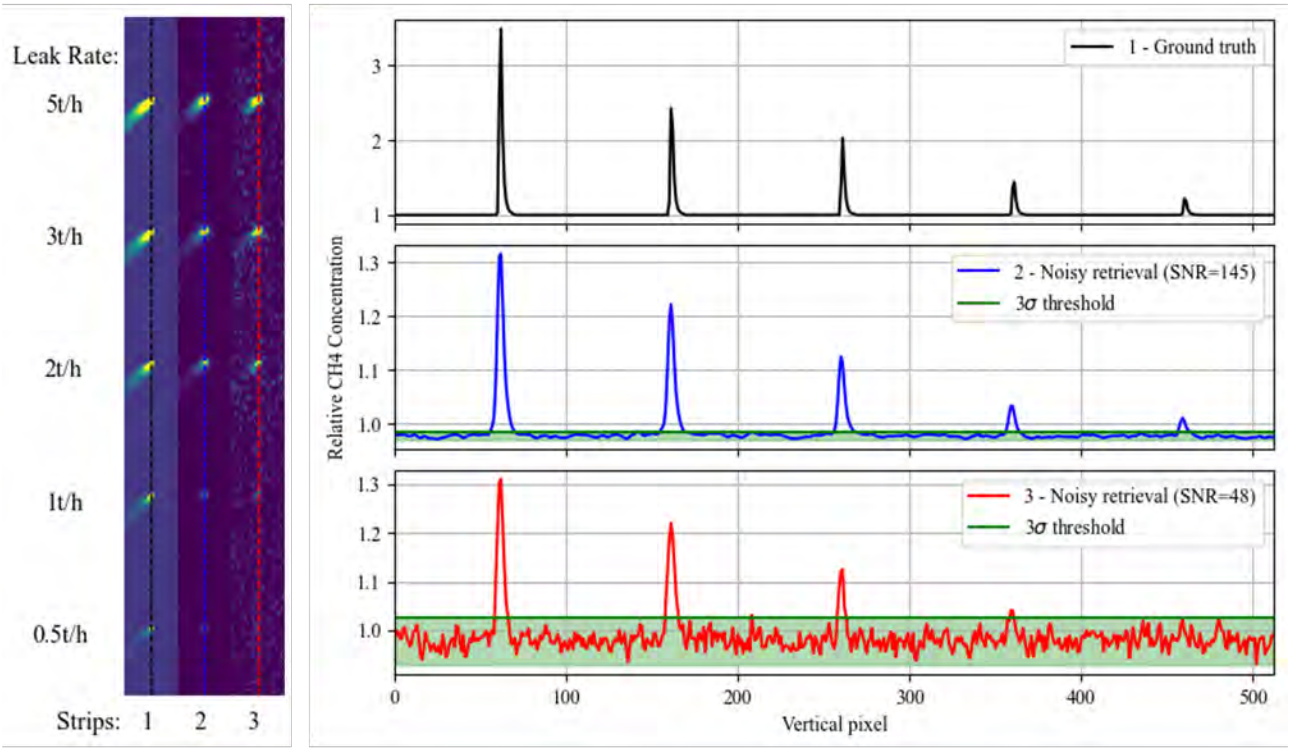

Figure 6: Plumes signal comparison between the ground truth, the retrieval from the frames with nominal noise performance (SNR=145), and the retrieval from frames with three times more noise (SNR=48). The strips shown on the left plot correspond to the middle column of the plume grid. The green areas indicate the 3σ interval from the computed background mean.

PRISMA, thereby providing significantly enhanced coverage in a single pass. Moreover, distinguishing itself, FINIS stands as the lightest space-based methane sensor, under 1 kg of mass, signifying its remarkable compactness and versatility.

Table 3: Point source detection thresholds for different instruments

Instrument	Mass (kg)	Pixel Size (m×m)	Swath (km)	Precision (%)	Detection threshold (t h^{-1})	Ref.
TROPOMI	230	5500×7000	2600	0.8	10	[14] [15]
MethaneSAT	183	100×400	200	0.1 – 0.2	0.5	[16] [17]
GHGSat	6	25×25	12	1.5	0.2	[6] [18]
PRISMA	80	30×30	30	3 – 9	0.5 – 2	[19] [20]
FINIS	**0.9**	**150×205**	**96**	**2 – 5**	**0.5 – 2**	[4]

4 METHANE CELL CALIBRATION

The methane cell calibration is an important validation step in the development of this new methane sensor. This test assesses the instrument's spectrum response to the methane absorption lines, enabling the assessment of the instrument's spectrum resolution and the verification of the CWL mapping across the FPA.

In this test, after removing the air using a vacuum pump, a 10 cm gas cell was filled with chemically pure methane at a specific pressure and placed between the sensor and the target. Fig. 7 shows the laboratory setup utilized during the calibration of CAM1. The target was illuminated by a halogen lamp powered by an AC voltage source. To mitigate stray light, additional baffles were employed to

cover both the methane cell and the instrument. To avoid reflection from the methane cell windows, the cell was placed with approximately 10° of inclination angle relative to the optical axis, which reduced the effective path length to 9.85 cm.

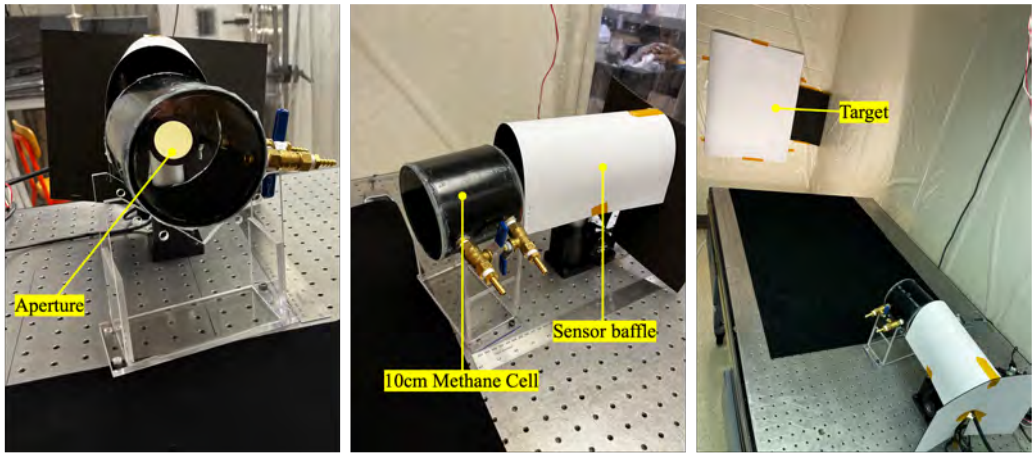

Figure 7: Methane cell calibration setup showing CAM1 under test

The transmission was computed by taking the ratio of the mean target frame, captured with the gas cell filled with a known methane pressure, to the mean control frame, which was taken with the cell filled only with air at ambient pressure. All frames were first corrected by removing the mean dark counts. A total of 100 frames were captured and averaged to form the mean frames for each case. Fig. 8 presents the modeled transmission (left) and the measured transmission (right) for the 10 cm methane cell at 10 psi of absolute pressure. The blue arc indicates the main methane absorption feature centered around 1666 nm. The weaker absorption features visible as faded arcs on the bottom of the model transmission are less visible in the measured transmission due to noise and unwanted effects caused by the AC light source.

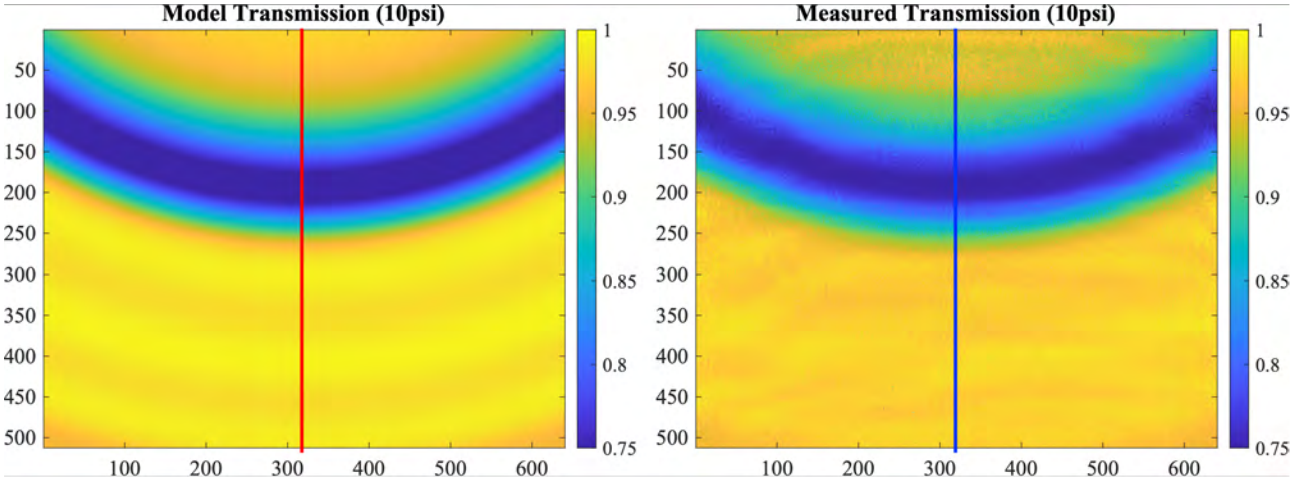

Figure 8: Methane cell calibration results for a 10 cm cell at 10 psi of methane, 23°C. (Left) Modeled transmission based on the modeled spectral response. (Middle) Measured transmission

For better comparison, Fig. 9 displays the middle vertical cross-section of the modeled and measured transmission across the FPA. This comparison allows us to verify that the filter bandwidth and the CWL mapping are sufficiently aligned with the predictions, with small deviations explained by the impressions in the tilt angle of the IF. Some of the low spatial frequency fluctuations observed in the measured transmission can be attributed to aliasing caused by the 60Hz fluctuation of the AC light source. Future tests will be conducted using a DC-powered light source to mitigate these unwanted features.

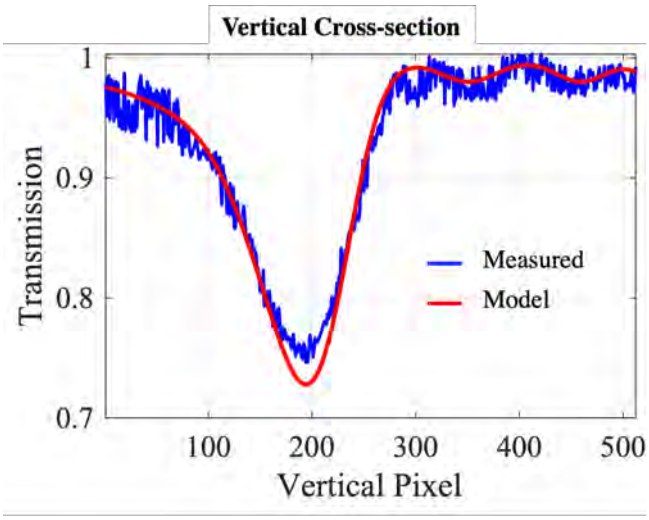

Figure 9: Vertical cross-section of the modeled and measured transmission for the 10cm methane cell test at 10 psi

5 UPCOMING FLIGHT IN THE ACMES MISSION

Along with FINIS, the ACMES satellite, shown in Fig. 10, will also host another USU student-led research project known as the Planer Langmuir/Impedance Diagnostic (PLAID). PLAID is a surface-mounted impedance probe designed for ionospheric studies. The current iteration of PLAID incorporates enhancements over its predecessor, which was deployed aboard the joint Brazil-US SPORT Mission, a 6U CubeSat launched from the ISS in 2022 [21]. The primary objective of ACMES is to demonstrate a novel active thermal management system featuring a deployable radiator named Active Thermal Architecture (ATA, [22]). ATA will support the cryogenic operation of an enhanced version of the Hyperspectral Thermal Imager (HyTI 2.0, [23]).

As secondary payloads, the FINIS and PLAID projects offered a total of 17 USU students the chance to actively contribute to NASA's endeavors in exploration and scientific research while simultaneously propelling nanosatellite technologies forward for atmospheric and space weather measurements, respectively. The FINIS project enlisted the involvement of 9 students, each lending their expertise throughout various developmental stages. Despite being primarily composed of undergraduate students, the FINIS team also had representation from both master's and PhD candidates. Similarly, in the PLAID project, a group of 8 students enthusiastically embraced this opportunity, with 6 advancing from undergraduate to master's studies and one embarking on a PhD journey, highlighting the diverse academic engagement fostered by these initiatives.

ACMES is planned to be launched by the end of 2025 into a 550 km altitude sun-synchronous circular orbit, with the local time of the ascending node (LTAN) between 10:00 a.m. and 11:30 a.m., local solar time. The advanced 16U bus is currently under development by Orion Space Solutions. It is equipped with 230W high-powered solar arrays and an onboard propulsion system, which can provide up to four years of mission lifetime over 400km altitude. Additionally, the spacecraft will transmit over 180 GB per day using KSATlite ground stations located at high latitudes. [3]

During the initial year of the ACMES mission, FINIS measurements will undergo validation by gathering data over specific target regions. These regions include locations where stations of the Total Carbon Column Observing Network (TCCON) are situated or where other missions have previously reported the presence of consistent methane plumes. After measurement corrections and validation, FINIS will continue collecting data over continental regions with SZA lower than 60 degrees until decommissioning.

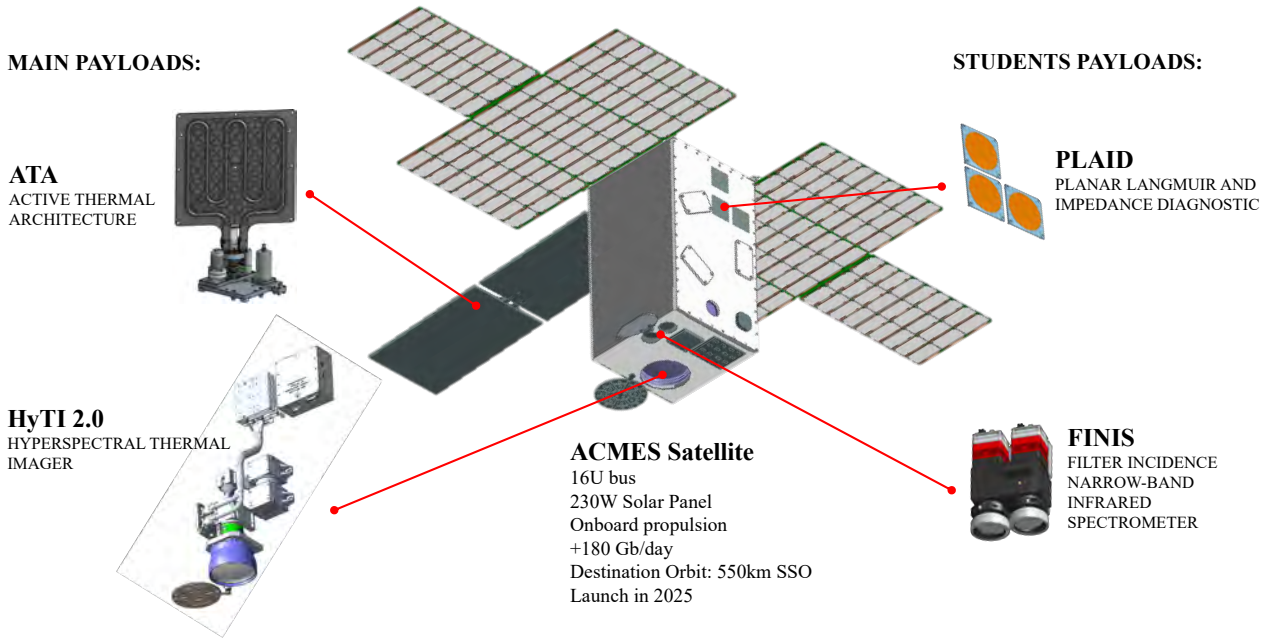

Figure 10: Main payloads and students lead research projects on upcoming ACMES mission

6 CONCLUSION

In this paper, we have presented updates on the development of FINIS, a compact imaging spectrometer designed for methane plume detection. Through innovative design elements such as the use of tilted interference filters in a binocular configuration, FINIS offers a competitive methane measurement capability in terms of precision, spatial resolution, and ground coverage while maintaining a much more compact form factor than other similar purposed space-based infrared spectrometers. Despite the small size, FINIS also features an integrated onboard calibration unit that enables dark frame and flat fielding calibration, essential for accurate data collection.

We have also discussed the fast retrieval method for methane plume detection, showcasing promising simulation results that demonstrate FINIS's capability to pinpoint plumes of varying sizes. In the case of the nominal radiometric performance, the simulation shows that even plumes originating from a leak rate of 500 kg/h can be potentially detected with a higher than 3σ confidence level, considering 5 km/h of near-surface wind speed. In the worst-case simulation, where the SNR performance is three times lower than the nominal performance, plumes over 2 t/h can be detected under the same atmospheric conditions. Although the simulation considers clear sky conditions and simplifies the plume concentration distribution using the Gaussian model, it serves as a first estimation of FINIS performance in detecting localized methane enhancements and provides insights on possible issues caused by the frames registration and retrieval method.

Additionally, the methane cell calibration results validate the instrument's spectral response and CWL mapping, laying the groundwork for further validation and testing. Looking ahead, the upcoming deployment of FINIS aboard the ACMES satellite, set for launch in 2025, represents a significant milestone for the project as it enters the space validation phase. The inclusion of FINIS and PLAID in the ACMES mission as student-led research projects underscores the support from NASA's Earth Science Technology Office (ESTO) for the active involvement of students in advancing cutting-edge technologies for climate science and space weather applications. This collaborative effort highlights the importance of engaging the next generation of scientists and engineers in the development of innovative solutions to address pressing environmental and scientific challenges.

REFERENCES

[1] K. Thoning, E. Dlugokencky, X. Lan, and NOAA Global Monitoring Laboratory, "Trends in globally-averaged CH4, N2O, and SF6," 2022. [Online]. Available: https://gml.noaa.gov/ccgg/trends_doi.html

[2] G. Myhre, D. Shindell, F.-M. Bréon, W. Collins, J. Fuglestvedt, J. Huang, D. Koch, J.-F. Lamarque, D. Lee, B. Mendoza, T. Nakajima, A. Robock, G. Stephens, H. Zhang, B. Aamaas, O. Boucher, S. B. Dalsøren, J. S. Daniel, P. Forster, C. Granier, J. Haigh, O. Hodnebrog, J. O. Kaplan, G. Marston, C. J. Nielsen, B. C. O'Neill, G. P. Peters, J. Pongratz, V. Ramaswamy, R. Roth, L. Rotstayn, S. J. Smith, D. Stevenson, J.-P. Vernier, O. Wild, P. Young, D. Jacob, A. R. Ravishankara, and K. Shine, "8 Anthropogenic and Natural Radiative Forcing," Tech. Rep.

[3] Charles Swenson, Lucas Anderson, Chad Fish, Bruno Mattos, Robert Wright, and Mark Schoeberl, "The Active Cooling for Multispectral Earth Sensors (ACMES) Mission," Portugal, 2022. [Online]. Available: https://az659834.vo.msecnd.net/eventsairwesteuprod/production-atpi-public/c7baeb9d67d4402fa8fa853889369bc8

[4] B. Mattos, M. Kirk, A. Marchant, C. Swenson, S. Brezenski, L. Anderson, C. Fish, J. Noto, J. Powell, N. Wallace, and M. Schoeberl, "Spectrometer for Methane Monitoring Using a Tilted Interference Filter," in *IGARSS 2023 - 2023 IEEE International Geoscience and Remote Sensing Symposium*, Jul. 2023, pp. 2410–2413, iSSN: 2153-7003. [Online]. Available: https://ieeexplore.ieee.org/document/10282162

[5] R. G. Sellar and G. D. Boreman, "Comparison of relative signal-to-noise ratios of different classes of imaging spectrometer," *Applied Optics*, vol. 44, no. 9, pp. 1614–1624, Mar. 2005, publisher: Optica Publishing Group. [Online]. Available: https://opg.optica.org/ao/abstract.cfm?uri=ao-44-9-1614

[6] D. Jervis, J. McKeever, B. O. A. Durak, J. J. Sloan, D. Gains, D. J. Varon, A. Ramier, M. Strupler, and E. Tarrant, "The GHGSat-D imaging spectrometer," *Atmospheric Measurement Techniques*, vol. 14, no. 3, pp. 2127–2140, Mar. 2021. [Online]. Available: https://amt.copernicus.org/articles/14/2127/2021/

[7] H. Hu, O. Hasekamp, A. Butz, A. Galli, J. Landgraf, J. Aan de Brugh, T. Borsdorff, R. Scheepmaker, and I. Aben, "The operational methane retrieval algorithm for TROPOMI," *Atmospheric Measurement Techniques*, vol. 9, no. 11, pp. 5423–5440, Nov. 2016. [Online]. Available: https://amt.copernicus.org/articles/9/5423/2016/

[8] C. Staebell, K. Sun, J. Samra, J. Franklin, C. Chan Miller, X. Liu, E. Conway, K. Chance, S. Milligan, and S. Wofsy, "Spectral Calibration of the MethaneAIR Instrument," Gases/Remote Sensing/Instruments and Platforms, preprint, Jan. 2021. [Online]. Available: https://amt.copernicus.org/preprints/amt-2020-513/amt-2020-513.pdf

[9] C. L. Weisberg, D. J. Preston, P. Z. Mouroulis, D. W. Wilson, D. R. Ardila, S. R. Zandbergen, C. L. Bradley, and R. O. Green, "Measured efficiency of three diffraction grating designs for the Carbon Plume Mapper (CPM) spectrometer," in *Imaging Spectrometry XXVI: Applications, Sensors, and Processing*, vol. 12688. SPIE, Nov. 2023, pp. 128–135. [Online]. Available: https://www.spiedigitallibrary.org/conference-proceedings-of-spie/12688/126880H/Measured-efficiency-of-three-diffraction-grating-designs-for-the-Carbon/10.1117/12.2692385.full

[10] S. Cogliati, F. Sarti, L. Chiarantini, M. Cosi, R. Lorusso, E. Lopinto, F. Miglietta, L. Genesio, L. Guanter, A. Damm, S. Pérez-López, D. Scheffler, G. Tagliabue, C. Panigada, U. Rascher, T. P. F. Dowling, C. Giardino, and R. Colombo, "The PRISMA imaging spectroscopy mission: overview and first performance analysis," *Remote Sensing of Environment*, vol. 262, p. 112499, Sep. 2021. [Online]. Available: https://www.sciencedirect.com/science/article/pii/S0034425721002170

[11] C. D. Rodgers, *Inverse methods for atmospheric sounding: theory and practice*, repr ed., ser. Series on atmospheric, oceanic and planetary physics. Singapore: World Scientific, 2008, no. 2.

[12] V. Rozanov, M. Buchwitz, K.-U. Eichmann, R. Beek, and J. Burrows, "SCIATRAN - A new radiative transfer model for geophysical applications in the 240-2400 NM spectral region: The pseudo-spherical version," *Advances in Space Research - ADV SPACE RES*, vol. 29, pp. 1831–1835, Jun. 2002.

[13] F. Pasquill, *Atmospheric diffusion: the dispersion of windborne material from industrial and other sources*, 2nd ed. Chichester: Horwood [u.a.], 1974.

[14] Instrumental Payload - Sentinel-5P Mission - Sentinel Online. [Online]. Available: https://sentinels.copernicus.eu/web/sentinel/missions/sentinel-5p/instrumental-payload

[15] T. Lauvaux, C. Giron, M. Mazzolini, A. d'Aspremont, R. Duren, D. Cusworth, D. Shindell, and P. Ciais, "Global assessment of oil and gas methane ultra-emitters," *Science*, vol. 375, no. 6580, pp. 557–561, Feb. 2022, publisher: American Association for the Advancement of Science. [Online]. Available: https://www.science.org/doi/10.1126/science.abj4351

[16] "MethaneSAT." [Online]. Available: https://www.methanesat.org/satellite/

[17] D. J. Jacob, D. J. Varon, D. H. Cusworth, P. E. Dennison, C. Frankenberg, R. Gautam, L. Guanter, J. Kelley, J. McKeever, L. E. Ott, B. Poulter, Z. Qu, A. K. Thorpe, J. R. Worden, and R. M. Duren, "Quantifying methane emissions from the global scale down to point sources using satellite observations of atmospheric methane," Apr. 2022. [Online]. Available: https://acp.copernicus.org/preprints/acp-2022-246/acp-2022-246.pdf

[18] E. D. Sherwin, J. S. Rutherford, Y. Chen, S. Aminfard, E. A. Kort, R. B. Jackson, and A. R. Brandt, "Single-blind validation of space-based point-source detection and quantification of onshore methane emissions," *Scientific Reports*, vol. 13, no. 1, p. 3836, Mar. 2023. [Online]. Available: https://www.nature.com/articles/s41598-023-30761-2

[19] D. Labate, M. Ceccherini, A. Cisbani, V. De Cosmo, C. Galeazzi, L. Giunti, M. Melozzi, S. Pieraccini, and M. Stagi, "The PRISMA payload optomechanical design, a high performance instrument for a new hyperspectral mission," *Acta Astronautica*, vol. 65, no. 9, pp. 1429–1436, Nov. 2009. [Online]. Available: https://www.sciencedirect.com/science/article/pii/S0094576509002173

[20] L. Guanter, I. Irakulis-Loitxate, J. Gorroño, E. Sánchez-García, D. H. Cusworth, D. J. Varon, S. Cogliati, and R. Colombo, "Mapping methane point emissions with the PRISMA spaceborne imaging spectrometer," *Remote Sensing of Environment*, vol. 265, p. 112671, Nov. 2021. [Online]. Available: https://linkinghub.elsevier.com/retrieve/pii/S0034425721003916

[21] L. Shibuya Sato, L. Loures, V. Costa, R. Wottrich, A. Jeronymo, H. Júnior, P. Cabral, R. Menezes, M. Oliveira, T. Carvalho, E. Oliveira, D. Vieira, C. Swenson, J. Casas, L. Krause, and J. Costa, "Lessons Learned During Testing Through Commissioning of the Joint Brazil-US SPORT Mission," *Small Satellite Conference*, Aug. 2023. [Online]. Available: https://digitalcommons.usu.edu/smallsat/2023/all2023/57

[22] L. Anderson, M. Kirk, B. Mattos, C. Swenson, C. Fish, M. Nunes, and R. Wright, “Active Thermal Control for the Multispectral Earth Sensors (ACMES) Mission,” in *Small Satellite Conference*, Aug. 2022. [Online]. Available: https://digitalcommons.usu.edu/smallsat/2022/all2022/169

[23] R. Wright, P. Lucey, L. Flynn, M. Nunes, T. George, S. Gunapala, D. Ting, and S. Rafol, “HYTI: Thermal Hyperspectral Imaging From a Cubesat Platform,” in *Small Satellite Conference*, Aug. 2019. [Online]. Available: https://digitalcommons.usu.edu/smallsat/2019/all2019/70